

# 3D MedDiffusion: A 3D Medical Diffusion Model for Controllable and High-quality Medical Image Generation

Haoshen Wang, Zhentao Liu, Kaicong Sun, Xiaodong Wang, Dinggang Shen, *Fellow, IEEE*, Zhiming Cui

**Abstract**—The generation of medical images presents significant challenges due to their high-resolution and three-dimensional nature. Existing methods often yield suboptimal performance in generating high-quality 3D medical images, and there is currently no universal generative framework for medical imaging. In this paper, we introduce the 3D Medical Diffusion (3D MedDiffusion) model for controllable, high-quality 3D medical image generation. 3D MedDiffusion incorporates a novel, highly efficient Patch-Volume Autoencoder that compresses medical images into latent space through patch-wise encoding and recovers back into image space through volume-wise decoding. Additionally, we design a new noise estimator to capture both local details and global structure information during diffusion denoising process. 3D MedDiffusion can generate fine-detailed, high-resolution images (up to 512x512x512) and effectively adapt to various downstream tasks as it is trained on large-scale datasets covering CT and MRI modalities and different anatomical regions (from head to leg). Experimental results demonstrate that 3D MedDiffusion surpasses state-of-the-art methods in generative quality and exhibits strong generalizability across tasks such as sparse-view CT reconstruction, fast MRI reconstruction, and data augmentation.

**Index Terms**—3D Medical Image Generation, Stable Diffusion Model, Patch-Volume Autoencoder, Noise Estimator.

## I. INTRODUCTION

GENERATIVE artificial intelligence (AI) has led to remarkable breakthroughs in recent years, driving substantial advancements across various domains and applications. Specifically, it has significantly contributed to progress in medical imaging and healthcare, with immense potential for future innovations. Generative AI have shown strong capabilities in various medical applications including image translation [1], segmentation [2], and the reconstruction of Computed Tomography (CT) [3] and Magnetic Resonance (MR) images [4].

Different kinds of generative models have shaped such rapid advancement including Variational Autoencoders (VAE) [5],

normalizing flows [6], Generative Adversarial Networks (GAN) [7], and Denoising Diffusion Probabilistic Model (DDPM) [8]. VAEs and normalizing flows are likelihood-based models, which explicitly model the data distribution and are theoretically well-founded. However, they often produce relatively modest generative results. On the other hand, GANs are non-probabilistic models that utilize an adversarial training approach. This method can result in training instability, characterized by issues such as mode collapse [9]. DDPM addresses these limitations by utilizing a diffusion process, modeled as a Markov chain [8]. Noise is incrementally added to the data, and a model is trained to reverse this process to generate samples. This method ensures stable training, producing high-quality, diverse outputs while offering a interpretable generative process. Large-scale models like stable diffusion [10] are widely applied in natural image domains and easily adapted for tasks such as image inpainting [11], and super-resolution [12].

Despite recent advancements, several challenges continue to impede the broader application of generative models in medical imaging. First, adapting computer vision algorithms to medical imaging is challenging due to its three-dimensional nature, which introduces significant computation overhead. Existing generative models in the medical domain are often limited in both resolution and quality [13]–[15]. Many of them rely on slice-wise 2D generation, while clinical practice needs 3D volumetric imaging. Second, the lack of efficient and controllable generation mechanisms forces the development of task-specific models, thereby increasing development costs.

We propose 3D Medical Diffusion (3D MedDiffusion), a large-scale 3D generative model designed for high-fidelity generation of medical images. First, 3D MedDiffusion introduces a novel Patch-Volume Autoencoder that compresses high-resolution images into low-resolution latent representations via a patch-wise encoder and recovers the entire image with a volume-wise decoder. Patch-wise encoding reduces the computational overhead of volume-wise encoding by exploiting the local properties in 3D medical images, while volume-wise decoding ensures artifact-free reconstruction results. Second, we design a novel noise estimator (named BiFlowNet) to replace the standard U-Net [16] in diffusion model. This module combines intra-patch and inter-patch flows to process both local (patch-wise) and global (volume-wise) information. The dual flow structure is crucial for reconstructing local details from noise while preserving global structure information. Furthermore, 3D MedDiffusion is trained on a comprehensive

Haoshen Wang, Zhentao Liu, Kaicong Sun, Dinggang Shen and Zhiming Cui are with the School of Biomedical Engineering & State Key Laboratory of Advanced Medical Materials and Devices, ShanghaiTech University, Shanghai, 201210, China. Dinggang Shen is also with Shanghai United Imaging Intelligence Co., Ltd., Shanghai, 200230, China, and Shanghai Clinical Research and Trial Center, Shanghai, 201210, China. (e-mail: {wanghsh2022, liuzht2022, sunkc, dgshen, cuizhm}@shanghaitech.edu.cn). (*Corresponding author: Zhiming Cui.*)

Xiaodong Wang is with United Imaging Healthcare Co., Ltd., Shanghai, 201807, China (e-mail: xiaodong.wang@united-imaging.com).

and diverse collection of 3D medical image datasets, covering both CT and MRI modalities and multiple anatomical regions from head to leg. Notably, ControlNet can be seamlessly integrated with the pre-trained 3D MedDiffusion model, enabling efficient fine-tuning for various downstream tasks. In this study, we evaluate 3D MedDiffusion on its generative performance and its effectiveness in downstream tasks: sparse-view CT reconstruction, fast MRI reconstruction, and data augmentation for segmentation. 3D MedDiffusion outperforms existing methods, demonstrating superior performance.

## II. RELATED WORK

### A. Medical Image Generation

Medical image generation is promising to address several clinical tasks, such as modality translation, CT enhancement, and MR acceleration. Existing research has explored the application of GAN-based methods for generating 3D medical images. Jin et al. [17] introduced an autoencoding GAN to generate 3D brain MRI images. Cirillo et al. [18] proposed a 3D model conditioned on multi-channel 3D brain MR images to generate tumor masks for segmentation. Sun et al. [19] developed a GAN with a hierarchical design to address memory demands of generating high-resolution 3D images.

Nevertheless, the unstable training process inherent to GAN framework often results in mode collapse and low quality generation. Recently, many researchers have shifted their focus to diffusion models (DMs) due to their high fidelity generation and stable training [8]. Müller-Franzes et al. [20] proposed a conditional latent DM, demonstrating its promise for generating 2D medical images. Moghadam et al. [21] showed that DMs are capable of generating a wide range of histopathological images. However, 3D imaging is more prevalent in medical contexts. This task poses challenges due to the high computational complexity of DMs for three-dimensional data. Consequently, many researchers explored efficient methods for generating 3D medical images using DMs. Zhu et al. [14] developed 3D image generators using pseudo-3D architectures, addressing volumetric inconsistencies through refiners or tuning. Friedrich et al. [13] applied a diffusion model to wavelet-decomposed images for efficiency. Khader et al. [15] employed a latent DM combining an autoencoder and video DM to generate high-quality 3D CT and MR images. Guo et al. [22] introduced MAISI, a concurrent latent DM based framework that improves autoencoder efficiency via tensor-splitting parallelism. This method divides feature maps into smaller segments, enabling parallel processing across multiple GPUs or sequential processing on a single GPU. It resembles sliding window inference on feature space, so it produces less artifacts than directly applying it on image space. In contrast, our Patch-Volume Autoencoder follows a two-stage patch-wise and volume-wise training strategy, ensuring no boundary artifacts during single-GPU inference. Besides, we can also integrate tensor parallelism [23] for multi-GPU inference to accelerate the process.

### B. Medical Generative Model for Downstream Tasks

Medical generative models hold great promise for diverse downstream tasks. Recent studies have explored the data

augmentation with DMs, such as training conditional DMs to generate synthetic data from segmentation masks [22]. Other works have applied DMs to solve inverse problems, including CT reconstruction [24] and image-to-image translation [25]. However, most of these methods require dedicated training for specific tasks. In contrast, our method leverages ControlNet to eliminate task-specific training, enabling efficient fine-tuning for diverse downstream tasks.

## III. METHOD

Our approach consists of three key components: a Patch-Volume Autoencoder that compresses a 3D medical image into a compact latent space (Sec. III-A), a noise estimator architecture named BiFlowNet for the 3D medical diffusion model (Sec. III-B), and conditional generation with ControlNet for downstream tasks (Sec. III-C).

### A. Compact Latent Space for 3D Medical Image

To enable efficient 3D medical image generation, we develop a novel compression framework that maps high-resolution 3D volumes into a compact, semantically meaningful latent space. It facilitates more efficient diffusion process. Building upon VQ-GAN [26], we introduce Patch-Volume Autoencoder with a two-stage training strategy to address the challenges of 3D medical image compression (Fig. 1), offering three key advantages. **(1) Memory efficient.** The first stage compresses and reconstructs small, fine-detailed patches, overcoming memory limitations of processing entire volumes. **(2) Artifact-free reconstruction.** The second stage fine-tunes the joint decoder, enabling seamless full-volume reconstruction without patch boundary artifacts. **(3) Meaningful and compact representation.** The Vector Quantization (VQ) mechanism maps continuous representations to discrete codes in a learned codebook, capturing anatomical patterns and handling representation variations across anatomical regions.

**1) Patch-wise Training:** In the first stage, the 3D volume  $\mathbf{X} \in \mathbb{R}^{H \times W \times D}$  is divided into smaller patches  $\{\mathbf{x}_i \in \mathbb{R}^{h \times w \times d}\}_{i=1}^N$ , where  $N$  denoting the total number of patches. We process these patches in a patch-wise manner using a patch encoder  $\mathcal{E}$ , a patch decoder  $\mathcal{D}_P$ , a discrete and learnable codebook  $\mathcal{C} = \{\mathbf{c}_k \in \mathbb{R}^C\}_{k=1}^K$  with  $K$  denoting the number of codes.

First, for each patch  $\mathbf{x}_i$ , the patch encoder  $\mathcal{E}$  extracts the corresponding patch feature  $\mathbf{z}_i = \mathcal{E}(\mathbf{x}_i) \in \mathbb{R}^{M \times C}$ , where  $M$  denoting the number of codes. Second,  $\mathbf{z}_i$  would then be transformed into quantized patch feature  $\tilde{\mathbf{z}}_i \in \mathbb{R}^{M \times C}$  via vector quantization  $\mathcal{VQ}$ :

$$\tilde{\mathbf{z}}_i = \mathcal{VQ}(\mathbf{z}_i) : \left\{ \begin{array}{l} \mathbf{c}_q \in \mathcal{C} \rightarrow \tilde{\mathbf{z}}_i^m, \\ \text{where } q = \operatorname{argmin}_k \|\mathbf{z}_i^m - \mathbf{c}_k\|_2 \end{array} \right\}_{m=1}^M. \quad (1)$$

Third, the patch decoder  $\mathcal{D}_P$  produces the patch reconstruction  $\tilde{\mathbf{x}}_i = \mathcal{D}_P(\tilde{\mathbf{z}}_i) \in \mathbb{R}^{h \times w \times d}$  from the quantized patch feature  $\tilde{\mathbf{z}}_i$ .

**2) Volume-wise Training:** We fine-tune the patch decoder  $\mathcal{D}_P$  into a joint decoder  $\mathcal{D}_J$ , avoiding the need for individual patch processing and concatenation. It enables high-resolution reconstruction devoid of boundary artifacts.

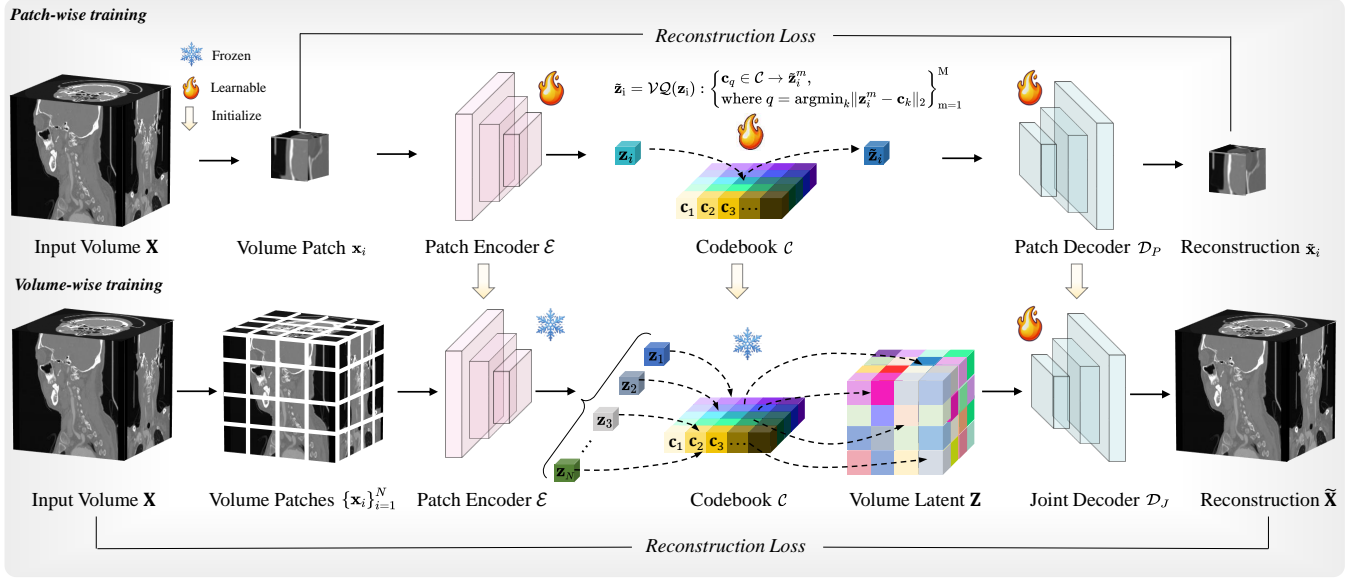


Fig. 1: Patch-Volume Autoencoder with a two-stage training strategy. In the first stage, the model is trained solely to compress and reconstruct small patches from high-resolution volumes. In the second stage, all parameters are fixed except for the decoder, which is fine-tuned on high-resolution volumes to become a joint decoder.

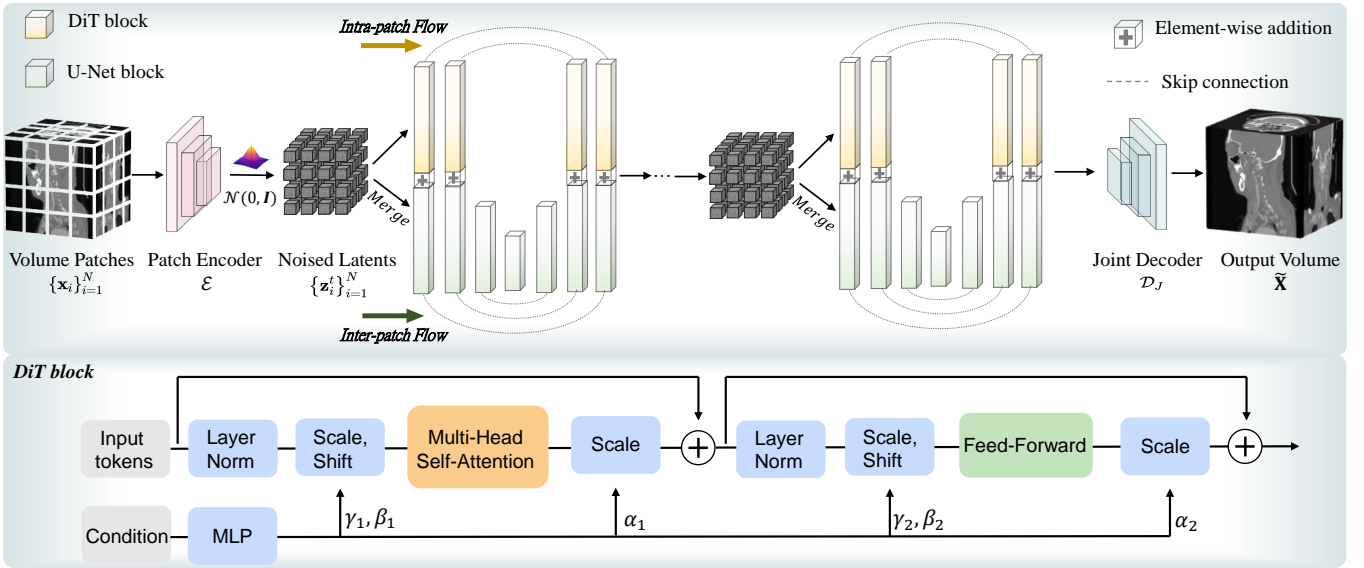


Fig. 2: BiFlowNet noise estimator. The intra-patch flow focuses on denoising each patch and recovering fine-grained local details, while the inter-patch flow is designed to capture and reconstruct the global structures across the entire volume.

As shown in Fig. 1, in this stage, the entire volume is first partitioned into smaller patches and each patch is then encoded and quantized to quantized patch features  $\{\tilde{z}_i\}_{i=1}^N$ , similarly to prior patch-wise training. Afterward, these quantized features are concatenated into a latent volume  $\tilde{\mathbf{Z}} \in \mathbb{R}^{N \cdot M \times C}$ , which is then decoded by the joint decoder  $\mathcal{D}_J$  to produce the final reconstruction  $\tilde{\mathbf{X}} = \mathcal{D}_J(\tilde{\mathbf{Z}}) \in \mathbb{R}^{H \times W \times D}$  at once. Notably, the parameters of the patch encoder  $\mathcal{E}$  and the codebook  $\mathcal{C}$  are initialized from patch-wise training stage and kept frozen during this stage, while the joint decoder  $\mathcal{D}_J$  being learnable. This approach is memory-efficient, as it only requires storing the backward gradients for the joint decoder,  $\mathcal{D}_J$ .

3) *Training Loss*: We use the same loss functions for both training stages. In this section, we use  $\mathbf{x}$  to replace either  $\mathbf{x}_i$

or  $\mathbf{X}$  and omit the dimensionality for simplicity. The complete reconstruction loss  $\mathcal{L}_{Rec}$  is formulated as:

$$\mathcal{L}_{Rec} = \mathcal{L}_{VQ} + \lambda_{Adv} \mathcal{L}_{Adv} + \lambda_{TP} \mathcal{L}_{TP}, \quad (2)$$

where  $\mathcal{L}_{VQ}$ ,  $\mathcal{L}_{Adv}$ , and  $\mathcal{L}_{TP}$  are vector quantization loss, adversarial loss and tri-plane loss, respectively.  $\lambda_{Adv}$  and  $\lambda_{TP}$  are loss weights for  $\mathcal{L}_{Adv}$  and  $\mathcal{L}_{TP}$ . Each loss function would be detailed in following.

$\mathcal{L}_{VQ}$  is the fundamental loss for Patch-Volume Autoencoder training [27], defined as:

$$\mathcal{L}_{VQ} = \|\mathbf{x} - \tilde{\mathbf{x}}\|_2 + \|\text{sg}[\mathcal{E}(\mathbf{x})] - \tilde{\mathbf{z}}\|_2 + \|\text{sg}[\tilde{\mathbf{z}}] - \mathcal{E}(\mathbf{x})\|_2, \quad (3)$$

where  $\tilde{\mathbf{x}}$  is the reconstruction counterpart of  $\mathbf{x}$ ,  $\tilde{\mathbf{z}}$  is the

quantized feature, and  $\text{sg}[\cdot]$  stands for stop-gradient operation. This loss function minimizes the disparity between input data  $\mathbf{x}$  and its reconstruction  $\tilde{\mathbf{x}}$ , while aligning encoded features  $\mathcal{E}(\mathbf{x})$  and feature codes  $\tilde{\mathbf{z}}$  searched from codebook  $\mathcal{C}$ .

$\mathcal{L}_{Adv}$  incorporates a discriminator  $\mathcal{D}$  to encourage more realistic reconstructions [26]:

$$\mathcal{L}_{Adv} = \log \mathcal{D}(\mathbf{x}) + \log(1 - \mathcal{D}(\tilde{\mathbf{x}})). \quad (4)$$

$\mathcal{L}_{TP}$  is employed to maintain high perceptual quality during vector quantization with help of perceptual loss [28]–[30]. In order to leverage existing 2D pre-trained feature extractor, we randomly select three orthogonal 2D planes from input data  $\{\mathbf{p}_n\}_{n=1}^3 \subset \mathbf{x}$  and reconstructed one  $\{\tilde{\mathbf{p}}_n\}_{n=1}^3 \subset \tilde{\mathbf{x}}$  at the same position to compute perceptual loss:

$$\mathcal{L}_{TP} = \sum_{n=1}^3 \|\phi(\mathbf{p}_n) - \phi(\tilde{\mathbf{p}}_n)\|_2, \quad (5)$$

where  $\phi$  is the pre-trained VGG-16 network [31], [32].

## B. 3D Medical Diffusion Model

1) *Diffusion Model*: The diffusion model in 3D MedDiffusion operates in the compact latent space, either patch-wise ( $\mathbf{x}_i$ ) or volume-wise ( $\mathbf{X}$ ). In this section, we use  $\mathbf{x}$  to denote both and omit dimensionality for simplicity. Diffusion model first defines a forward noising process that incrementally adds noise to the initial latent  $\mathbf{z}^0 = \mathcal{E}(\mathbf{x})$ , formulated as:

$$q(\mathbf{z}^t | \mathbf{z}^{t-1}) = \mathcal{N}(\mathbf{z}^t; \sqrt{1 - \beta^t} \mathbf{z}^{t-1}, \beta^t \mathbf{I}), \quad (6)$$

where  $\sqrt{1 - \beta^t} \mathbf{z}^{t-1}$  is the mean and  $\beta^t \mathbf{I}$  is the covariance of the distribution at timestep  $t \in \{1, 2, \dots, T\}$  with  $T$  denoting total timesteps.  $\mathbf{I}$  is the identity matrix and  $\beta_t \in (0, 1)$  is a noise-level hyper-parameter. For the reverse process, the diffusion model is trained to learn a denoising network  $\mu_\theta$ , denoted as:

$$p_\theta(\mathbf{z}^{t-1} | \mathbf{z}^t) = \mathcal{N}(\mathbf{z}^{t-1}; \mu_\theta(\mathbf{z}^t, t), \sigma^t \mathbf{I}), \quad (7)$$

here  $\mu_\theta(\mathbf{z}^t, t)$  and  $\sigma^t \mathbf{I}$  are the mean and covariance. The training objective is to train a noise estimator  $\epsilon_\theta$  to predict the added Gaussian noise  $\epsilon$ , described by the following loss function:

$$\mathcal{L} = \mathbb{E}_{\mathbf{z}^0, \epsilon, t, \mathbf{c}} \left[ \|\epsilon - \epsilon_\theta(\mathbf{z}^t, t, \mathbf{c})\|_2 \right], \quad (8)$$

where  $\mathbf{c}$  is the class condition, indicating the data modality and anatomical regions. Once  $p_\theta(\mathbf{z}^{t-1} | \mathbf{z}^t)$  is trained, new latents can be generated by progressively sampling  $\mathbf{z}^{t-1} \sim p_\theta(\mathbf{z}^{t-1} | \mathbf{z}^t)$ .

2) *BiFlowNet Architecture*: We propose a novel noise estimator called BiFlowNet, which integrates both intra-patch flow and inter-patch flow to generate latent representations. Intra-patch flow captures fine-grained details, whereas inter-patch flow maintains global structural consistency. The dual-flow latent features are integrated to achieve both objectives simultaneously.

**Intra-Patch Flow.** In our approach, high-resolution 3D medical images are encoded into latent space on patch-wise basis, resulting in each patch following an independent distribution. Intra-patch flow focuses on denoising each patch

and recovering fine-grained local details. We adopt diffusion transformer (DiT) [33] as the backbone for intra-patch flow, leveraging its exceptional performance in complex generative tasks on large datasets. Class embedding is also incorporated as input to enable multi-class training for different regions and modalities. The DiT block architecture follows the design in [33], with adaptations for 3D inputs such as expanded spatial dimensions, as shown in Fig. 2.

**Inter-Patch Flow.** However, generating only patch-wise regions fails to preserve global structural consistency when reconstructing the entire 3D volume. In response to this challenge, we design inter-patch flow to capture and reconstruct the global structures across the entire volume. We opt standard 3D U-Net [16] as the backbone to eliminate computation overhead raised from high-resolution 3D images.

**Dual Flow Integration.** As shown in Fig. 2, to avoid isolated optimization, we combine local and global features from dual flows with element-wise addition at each timestep. Features from DiT's first and last two blocks are merged with U-Net's corresponding blocks. The latent volume is then processed by the U-Net and divided into patches for the DiT at the next timestep.

## C. ControlNet for Downstream Tasks

To improve controllability and adaptability for diverse downstream tasks, we integrate ControlNet [34] into the diffusion model. ControlNet is specifically designed to inject additional task-specific conditions into the diffusion model via fine-tuning. In this process, the parameters of the pre-trained diffusion model are frozen, while a cloned, trainable encoder of BiFlowNet is introduced. This trainable copy accepts task-specific condition as input and its output is connected to the pre-trained diffusion model via zero convolutions [34]. Since the diffusion model in 3D MedDiffusion operates within the latent space, it is essential to encode the task-specific condition into this space, denoted as  $\mathbf{c}_{task}$ . The loss function for the fine-tuning process is defined as:

$$\mathcal{L} = \mathbb{E}_{\mathbf{z}^0, \epsilon, t, \mathbf{c}, \mathbf{c}_{task}} \left[ \|\epsilon - \epsilon_\theta(\mathbf{z}^t, t, \mathbf{c}, \mathbf{c}_{task})\|_2 \right]. \quad (9)$$

This control mechanism allows the 3D MedDiffusion to evolve from a generic generative model into a task-specific model by leveraging the pre-trained model's strong prior knowledge. Moreover, the fine-tuning process is notably time-efficient, as only a small set of parameters require training.

## IV. EXPERIMENTS

In this section, we begin by detailing the datasets (Sec. IV-A.1) and implementation details (Sec. IV-A.2). Next, we compare our 3D MedDiffusion with other competing methods (Sec. IV-B). Finally, we assess the generalizability of 3D MedDiffusion across three downstream tasks: sparse-view CT reconstruction, MRI reconstruction, and data augmentation for segmentation (Sec. IV-D).



## A. Experimental Setting

1) *Dataset*: To develop a large-scale 3D generative model, we train the 3D MedDiffusion on an extensive collection of high-quality 3D medical image datasets. These datasets include CT scans of head and neck, chest and abdomen, and lower limb, as well as MR images of brain, chest, abdomen, and knee, covering the major anatomical regions of the human body. We organize these multi-modality and region-mixed datasets into six sub-datasets: **CTHeadNeck**, **CTChestAbdomen**, **CTLowerLimb**, **MRBrain**, **MRChestAbdomen**, **MRKnee**. Both Patch-Volume Autoencoder and diffusion model are trained on these combined datasets, with diffusion model conditioned on data modalities and regions.

**CTHeadNeck Dataset**. For head and neck region of CT modality, we collect one public dataset and two in-house datasets. The public dataset is the CQ500 dataset [35] with 491 CT scans. The in-house datasets consist of a CTA dataset with 256 images and a CBCT dataset with 600 images. In total, we collect 1,347 images with image size ranging from  $256 \times 256 \times 128$  to  $256 \times 256 \times 256$  and voxel spacing below 1.25mm along three axes.

**CTChestAbdomen Dataset**. For chest and abdomen region of CT modality, we involve four public CT datasets: The Pulmonary Airway dataset [36]–[39] with 300 CT scans. The LIDC-IDRI dataset [40] with 1,010 CT scans. The CT-Spline1K dataset [41] with 1,005 CT scans. The AbdomenCT-1K dataset [42] with 1,112 CT scans. In all, we gather 3000 images after excluding low-quality ones with image size ranging from  $256 \times 256 \times 256$  to  $512 \times 512 \times 512$  and voxel spacing below 1.25mm along three axes.

**CTLowerLimb Dataset**. For lower limb region of CT modality, we develop an in-house dataset with 400 CT scans, covering the area from the thigh to the foot. The image size ranges from  $256 \times 256 \times 256$  to  $256 \times 256 \times 512$ , with voxel spacing below 1.25mm along three axes.

**MRBrain Dataset**. For brain region of MR modality, we collect 3000 MR images from the UK Biobank [43], comprising 1,500 T1-weighted images and 1,500 T2-weighted FLAIR images. Non-brain regions have been excluded to enhance model focus. All images have a size of  $192 \times 192 \times 192$  and a voxel spacing of 1mm along all three axes.

**MRChestAbdomen Dataset**. For chest and abdomen region of MR modality, we create an in-house dataset comprising 1,826 MR images, including both T1-weighted and T2-weighted data. All images have a size of  $256 \times 256 \times 128$  and a voxel spacing of 1.25mm along the  $x$ - and  $y$ -axes, and 2mm along the  $z$ -axis.

**MRKnee Dataset**. For knee region of MR modality, we use the publicly available fastMRI [44] dataset, focusing exclusively on single-coil data for model development. This dataset comprises 1172 volumes, each consisting of approximately 40 slices with size of  $320 \times 320$ . We interpolate the data along the  $z$ -axis, standardizing each volume to a size of  $320 \times 320 \times 64$ . All images have a voxel spacing of 1mm along the  $x$ - and  $y$ -axes, and 5mm along the  $z$ -axis.

2) *Implementation Details*: For Patch-Volume Autoencoder, during the patch-wise training phase, we set the patch size to  $64 \times 64 \times 64$ , with a compression ratio of  $4 \times 4 \times 4$ . The

TABLE I

Quantitative results on CT image generation.

	FID ↓	MS-SSIM ↓	MMD ↓
HA-GAN	0.0405	0.3816	1.1008
MedicalDiffusion	0.0284	<b>0.2238</b>	0.6500
WDM	0.0228	0.2313	0.4749
MAISI	0.0135	0.2713	0.2782
Ours	<b>0.0055</b>	0.2227	<b>0.1049</b>

TABLE II

Quantitative results on MRI image generation.

	FID ↓	MS-SSIM ↓	MMD ↓
HA-GAN	0.1284	0.7443	4.4638
MedicalDiffusion	0.0291	0.7847	1.9492
WDM	0.0057	0.7844	0.8742
MAISI	0.0075	0.7380	0.6957
Ours	<b>0.0044</b>	<b>0.7036</b>	<b>0.6372</b>

codebook contains 8192 codes with a dimensionality of 8. The training batch size is 8, the learning rate is  $3 \times 10^{-4}$ . And we start to train the discriminator after 20,000 iterations. In the volume-wise training phase, only the decoder and discriminator are trainable. The batch size is 1, and the learning rate is lowered to  $3 \times 10^{-5}$ . We set  $\lambda_{Adv} = 2$  and  $\lambda_{TP} = 4$  for both phases. The training for both phases was conducted on a single NVIDIA A100 GPU with 80 GB of memory. For Diffusion Model, we employ the cosine noise schedule [45] with  $T = 1000$  timesteps, the learning rate is  $1 \times 10^{-4}$  with polynomial learning rate decay, and batch size is 8. It is trained on eight NVIDIA A100 80G GPUs.

3) *Competing Methods*: We select several generative methods as baselines, including both GAN-based and diffusion-based approaches, as detailed below. HA-GAN [19] is a hierarchical amortized GAN which generates low-resolution images and high-resolution sub-volumes simultaneously to address memory constraints. Medical Diffusion [15] is a video diffusion model trained in the learned latent space of a 3D VQ-GAN. WDM [13] is a diffusion-based framework for medical image synthesis using wavelet-decomposed images. MAISI [22] is a 3D U-Net trained in the learned latent space of a 3D VAE. To ensure fair evaluation, we trained all methods from scratch. All comparisons are conducted on **CTChestAbdomen** and **MRbrain** datasets.

4) *Evaluation Metrics*: We evaluate the fidelity and diversity of generated images using Fréchet Inception Distance (FID) [46] and Maximum Mean Discrepancy (MMD) [47], which assess the similarity between the distributions of real and generated images. For feature extraction in FID and MMD calculations, we use a 3D ResNet model pre-trained on 3D medical images [48]. Lower FID and MMD values indicate higher realism of the generated images. Besides, we use the Multi-Scale Structural Similarity Index (MS-SSIM) to assess the diversity of the generated images. MS-SSIM measures the structural similarity between generated images across multiple scales, with lower values reflecting higher diversity.

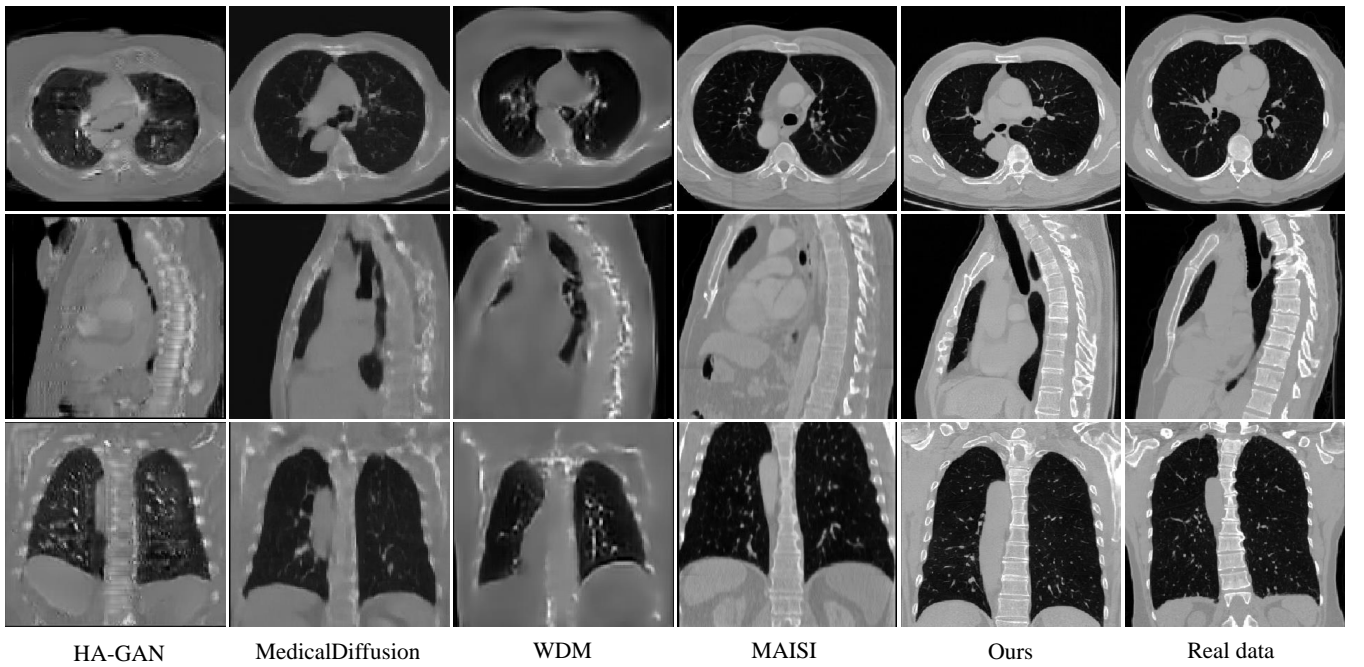


Fig. 3: Qualitative results on unconditional CT image generation. Window:  $[-1000, 1000]$  HU.

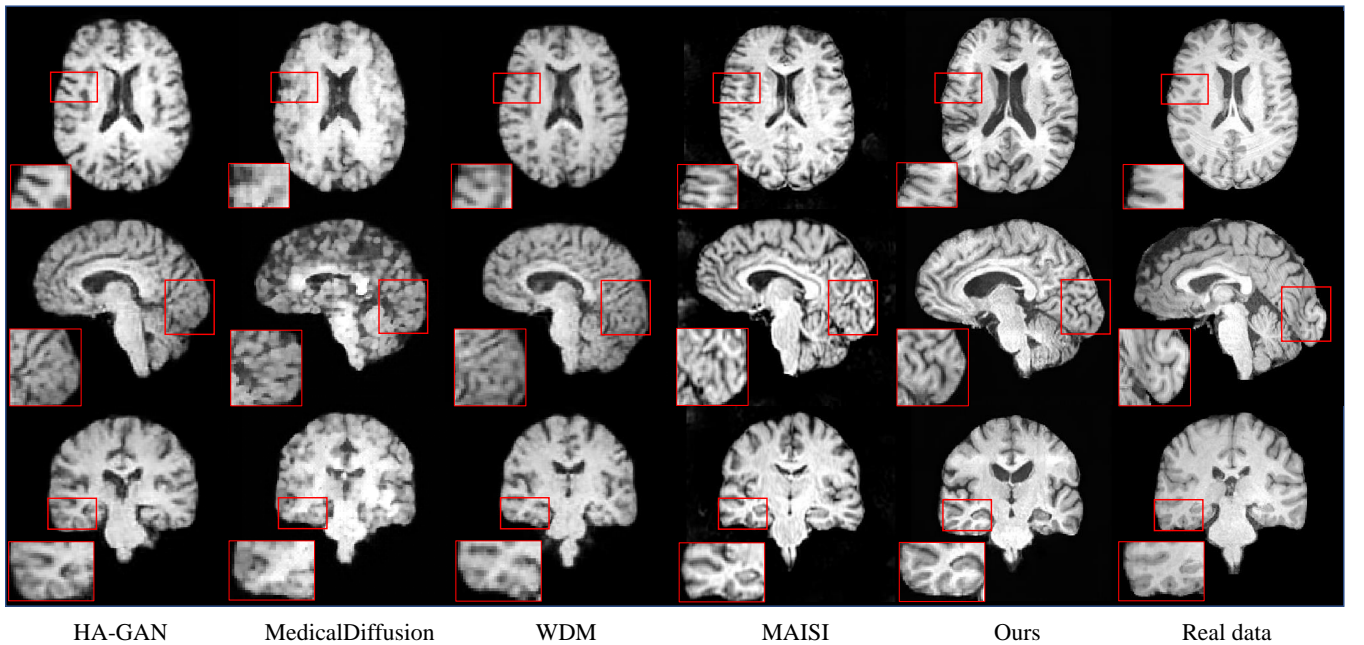


Fig. 4: Qualitative results on unconditional MR image generation.

## B. Comparison

1) *Quantitative Evaluation*: The quantitative experimental results for **CTChestAbdomen** dataset are provided in Tab. I. Our method achieves the lowest FID and MMD scores, demonstrating superior generative fidelity and realism. Compared to the second-best method, MAISI, our FID and MMD scores are more than two times lower, highlighting a significant improvement in generative fidelity. While MedicalDiffusion achieves the best performance in MS-SSIM metric, our method delivers comparable results. The quantitative experimental results for the **MRbrain** dataset are summarized in Tab. II. Our proposed method also achieves the best performance among

all the metrics by a considerable margin.

2) *Qualitative Evaluation*: To qualitatively evaluate the generation capabilities of all methods, we present some generated samples from **CTChestAbdomen** dataset (Fig. 3) and **MR-Brain** dataset (Fig. 4). It is evident that HA-GAN, MedicalDiffusion, and WDM struggle to produce high-resolution CT images, resulting in noisy and blurry outputs with insufficient details. MAISI produces satisfactory results but is slightly inferior to our method. In contrast, our proposed method excels in capturing fine details like vertebrae in CT images. It also produces sharp edges, such as the brain surface of MR images.

To further evaluate the authenticity of the generated images,

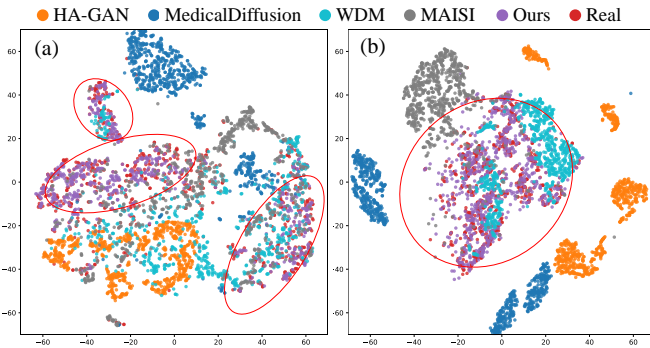


Fig. 5: t-SNE visualization on (a) **CTChestAbdomen** dataset and (b) **MRBrain** dataset. Features extracted from the generated images are embedded into a 2-dimensional space.

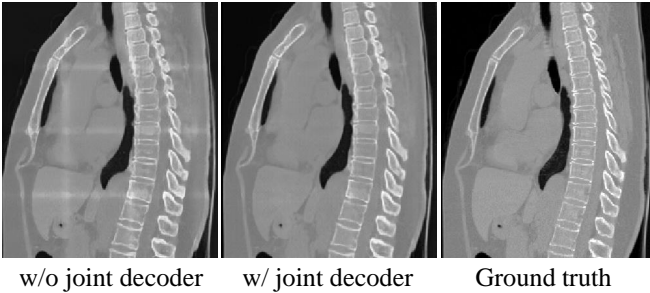


Fig. 6: Self-reconstruction results of ablation study on joint decoder. Window: [-1000, 1000] HU.

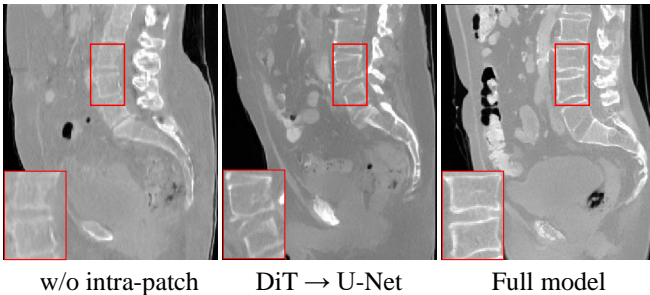


Fig. 7: Qualitative results of ablation study on BiFlowNet. Window: [-1000, 1000] HU.

we project the images into a high-dimensional embedding space and apply a dimensionality reduction technique to visualize the distributions. For comparison, we first employ a 3D pre-trained ResNet model [48] to extract features from 750 generated CT images for each method. We then apply t-SNE [49] to reduce the dimensionality to 2. This enables us to evaluate whether the generated distributions align with the real distributions in latent space. The resulting two-dimensional space is visualized in Fig. 5. We observe that our generated distribution (purple dots) aligns more closely and compactly with the real distribution (red dots), as highlighted by the red ellipses. This demonstrates the superiority of our method in generating realistic images.

### C. Ablation Study

In this section, we validate the effectiveness of two main components employed in our method, including Patch-Volume Autoencoder, and BiFlowNet noise estimator.

TABLE III

Quantitative results of ablation study on joint decoder

	PSNR (dB) $\uparrow$	SSIM $\uparrow$
w/o joint decoder	34.2307 (1.2492)	0.9273 (0.0925)
w/ joint decoder	35.7916 (1.2187)	0.9314 (0.0963)

TABLE IV

Quantitative results of ablation study on the BiFlowNet

	w/o intra-patch	DiT $\rightarrow$ U-Net	Full model
FID $\downarrow$	0.0117	0.0087	0.0055
MMD $\downarrow$	0.2392	0.1253	0.1049

1) *Patch-Volume Autoencoder*: Our method uses a two-stage training strategy for Autoencoder. In the first stage, entire network is trained in a patch-wise manner. In the second stage, the patch decoder is fine-tuned into a joint decoder in a volume-wise manner. The model cannot be trained in volume-wise alone due to the memory overhead. Therefore, we only assess the effectiveness of the joint decoder by comparing it to the patch-wise decoder for image compression and reconstruction. The experiment were conducted on the **CTChestAbdomen** dataset, with 30 images randomly selected as the test set. We calculated Peak Signal-to-Noise Ratio (PSNR) and Structural Similarity Index (SSIM) [50] between the original and reconstructed images, and the quantitative results are presented in Tab. III. Numbers outside parentheses denote the mean values, while those inside denote the standard deviations. The results indicate that incorporating joint decoder significantly enhances reconstruction quality across both metrics. Particularly, shown in Fig. 6, the joint decoder effectively eliminates patch boundary artifacts, which are commonly caused by patch-wise decoding.

2) *BiFlowNet*: To verify the effectiveness of our BiFlowNet design, we compare with two different settings: removing the intra-patch flow from the noise estimator, and replacing the DiT block of the intra-patch flow with a standard U-Net block. Note that, the model cannot be trained with intra-patch flow alone, as patch-wise generation is insufficient to produce meaningful reconstructions across the entire volume. These experiments were conducted on **CTChestAbdomen** dataset. We calculated FID and MMD metrics for evaluation. The experimental results are presented in Tab. IV and Fig. 7. The findings clearly demonstrate that capturing intra-patch information is crucial for fine-grained local details generation. DiT block is clearly more effective than U-Net, particularly for generative models trained on large-scale dataset.

### D. Downstream Tasks

The pre-trained generative model can be adapted to a variety of downstream tasks through integration with ControlNet. In this section, we assess its performance across three tasks: sparse-view CT reconstruction, fast MRI reconstruction and data augmentation for segmentation.

1) *Sparse-View CT Reconstruction*: In this experiment, we demonstrate the feasibility of leveraging the powerful generative prior knowledge learned by 3D MedDiffusion to address



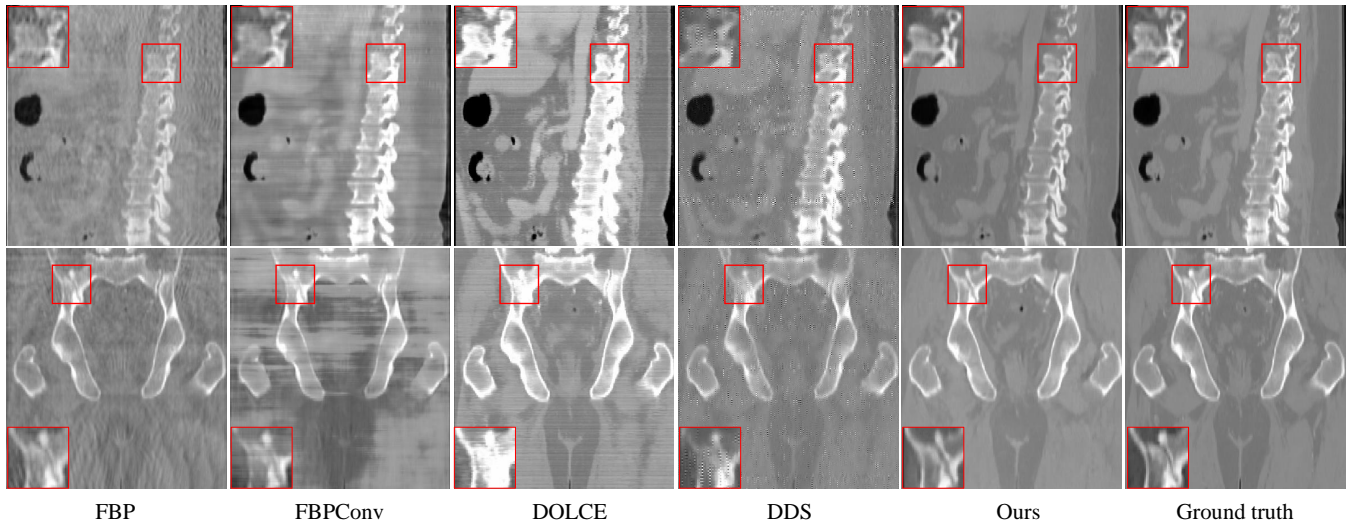


Fig. 8: Qualitative results of sparse-view CT reconstruction. Window:[-1000,000] HU.

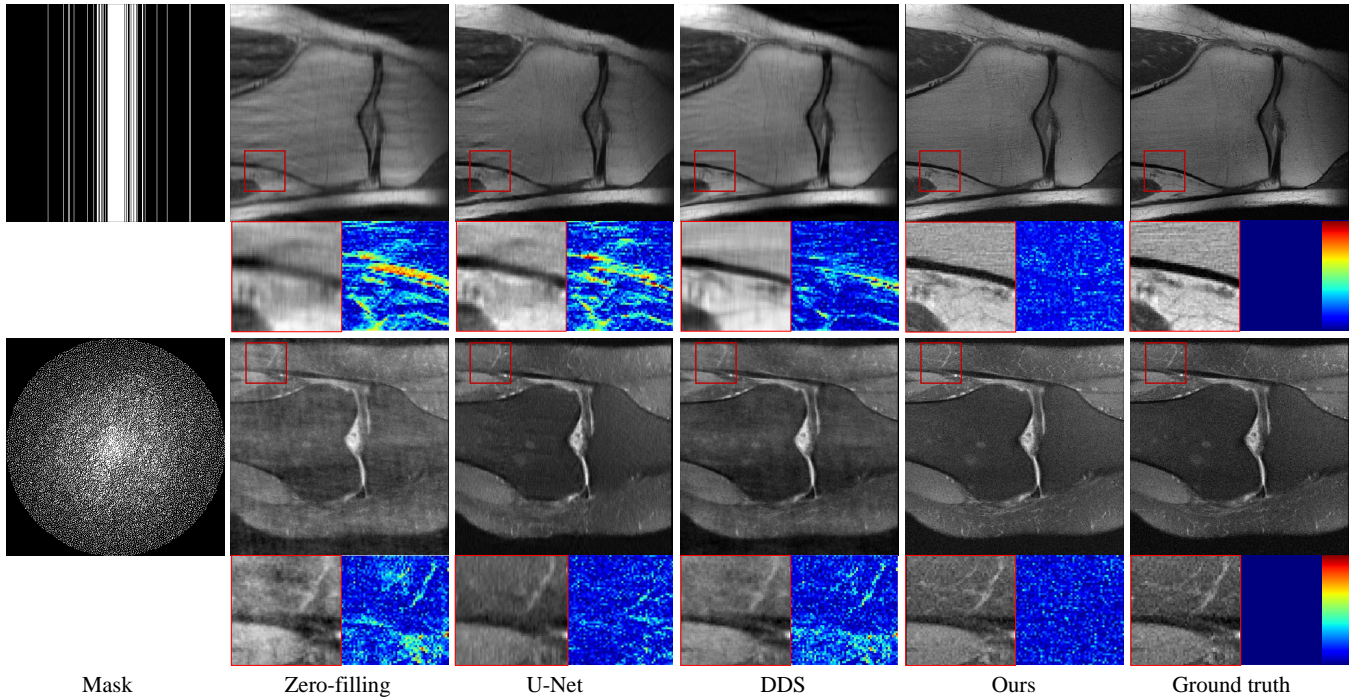


Fig. 9: Qualitative results of fast MRI reconstruction.

the sparse-view CT reconstruction. We conduct the experiment on a public dataset KiTs19 [51], which includes 210 Kidney CT scans. For each 3D CT volume, we uniformly render 40 views in a full circle with fan-beam geometry based on ASTRA-toolbox [52] and then perform reconstruction. Our pre-trained model is fine-tuned with ControlNet. The fine-tuning objective is defined in Eq. (9). The Filtered Back-Projection (FBP) [53] reconstruction results used as the condition input with the full-view reconstruction results serving as the ground truth. We compare our method with several existing approaches, including FBPCnv [54], DOLCE [3], and DDS [24], and report PSNR and SSIM metrics to evaluate performance. As shown in Tab. V, our proposed method achieves the highest scores across both metrics, demonstrating our effectiveness. Additionally, two representative cases are

presented in Fig. 8, where our reconstruction results deliver superior image quality and enhanced clarity of details.

2) *Fast MRI Reconstruction*: In this experiment, we aim to accelerate MRI reconstruction by leveraging pre-trained 3D MedDiffusion to map  $k$ -space downsampled reconstructions to fully-sampled reconstructions. We conduct the experiment on **MRKnee** dataset and compare our method against zero-filling, U-Net [54], and DDS [24]. PSNR and SSIM are used as evaluation metrics. We adopt two types of random downsampling masks including 1D Gaussian mask and Poisson mask, and the downsampling ratio is  $8\times$ . The quantitative results are summarized in Tab. VI, with two visualized examples of different downsampling masks presented in Fig. 9. Notably, our method achieves highest metric performance in both downsampling masks, and deliver superior reconstructions devoid of artifacts.



TABLE V

Quantitative results of sparse-view CT reconstruction.

	FBP	FBPConv	DOLCE	DDS	Ours
PSNR (dB) $\uparrow$	16.5327 (2.3140)	24.8138 (2.5968)	18.3710 (1.2488)	24.8110 (3.0709)	<b>27.9169</b> (4.1454)
SSIM $\uparrow$	0.6643 (0.1352)	0.7756 (0.1571)	0.7091 (0.1396)	0.6488 (0.1270)	<b>0.9297</b> (0.0313)

TABLE VI

Quantitative results of MRI reconstruction.

	Zero-filling	U-Net	DDS	Ours
PSNR (dB) $\uparrow$	29.4335 (1.8688)	33.5105 (2.2259)	30.4892 (1.8758)	<b>34.5374</b> (3.2673)
SSIM $\uparrow$	0.8717 (0.0308)	0.9107 (0.0453)	0.8847 (0.0374)	<b>0.9130</b> (0.0569)

Our volume-wise generation ensures better 3D consistency compared to the slice-wise generation of competing methods.

3) *Data Augmentation in Segmentation Task*: Deep learning-based medical image segmentation is often limited by insufficient training data. In this experiment, we leverage the strong generative capabilities of 3D MedDiffusion to augment data and enhance segmentation performance. We use a standard nnU-Net [55] for segmentation on KiTs19 dataset [51], which includes kidney and tumor regions. The testing set consist of 20 CT images and their segmentation masks, with the remaining 190 cases available for training. We define the following four training settings. **(1) 50% Real**: Randomly select 50% from the 190 cases as training data. **(2) 50% Real + 25% Synthesis**: Use (1) as the primary training data, then generate new CT images from half of selected cases using 3D MedDiffusion conditioned by their segmentation masks. **(3) 100% Real**: Use all 190 cases. **(4) 100% Real + 25% Synthesis**: Use all 190 cases and generate new CT images for 25% of selected cases. For evaluation, we conducted 5-fold cross-validation and use the 95% Hausdorff Distance (95HD) and Dice Similarity Coefficient (DSC) as comparative metrics. The overall quantitative results are presented in Fig. 10. Overall, the inclusion of synthetic data enhances segmentation results in both scenarios, whether the real data is limited (50% real) or sufficient (100% real). When real data is limited, the improvement is particularly substantial. Tumor segmentation shows a 6.14% increase in the Dice score, while the 95HD decreases by 20.66mm and kidney segmentation shows a 7.87mm reduction in 95HD. When real data is sufficient, synthetic data is also beneficial. For tumor segmentation, the standard deviation of the Dice score improves by 9.44%, while 95HD decreases by 1.02mm.

## V. CONCLUSION

In this paper, we introduce the 3D Medical Diffusion (3D MedDiffusion) model to generate high-quality 3D medical images. 3D MedDiffusion achieves its performance through two key design components: the Patch-Volume Autoencoder and the BiFlowNet noise estimator. Additionally, it can be effectively integrated with ControlNet, enabling efficient adaptation to a range of downstream tasks in medical scenarios. Our experiments demonstrate superior generative performance and strong generalizability across diverse tasks.

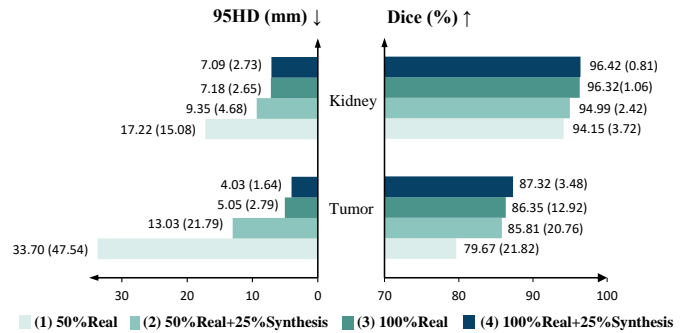


Fig. 10: Quantitative comparison on data augmentation.

Although achieved promising results, our method does have its limitations. First, it lacks the ability to produce images at arbitrary resolutions. Arbitrary-size generation could potentially be achieved with implicit neural encoder [56]. Second, our approach does not incorporate age and gender as conditioning factors for synthesizing medical images. Future work could explore the inclusion of additional conditions to enhance clinical applicability. Third, diffusion models require significant time and resources for generating high-resolution 3D medical images. We aim to design time- and memory-efficient one-step generation to improve practicality in future.

## REFERENCES

- [1] M. Özbey, O. Dalmaz, S. U. Dar, H. A. Bedel, Ş. Öztürk, A. Güngör, and T. Çukur, “Unsupervised medical image translation with adversarial diffusion models,” *IEEE Transactions on Medical Imaging*, 2023.
- [2] T. Amit, T. Shaharabany, E. Nachmani, and L. Wolf, “Segdiff: Image segmentation with diffusion probabilistic models,” *arXiv preprint arXiv:2112.00390*, 2021.
- [3] J. Liu, R. Anirudh, J. J. Thiagarajan, S. He, K. A. Mohan, U. S. Kamilov, and H. Kim, “Dolce: A model-based probabilistic diffusion framework for limited-angle ct reconstruction,” in *Proceedings of the IEEE/CVF International Conference on Computer Vision*, pp. 10498–10508, 2023.
- [4] C. Cao, Z.-X. Cui, Y. Wang, S. Liu, T. Chen, H. Zheng, D. Liang, and Y. Zhu, “High-frequency space diffusion model for accelerated mri,” *IEEE Transactions on Medical Imaging*, 2024.
- [5] D. P. Kingma, “Auto-encoding variational bayes,” *arXiv preprint arXiv:1312.6114*, 2013.
- [6] D. Rezende and S. Mohamed, “Variational inference with normalizing flows,” in *International conference on machine learning*, pp. 1530–1538, PMLR, 2015.
- [7] I. Goodfellow, J. Pouget-Abadie, M. Mirza, B. Xu, D. Warde-Farley, S. Ozair, A. Courville, and Y. Bengio, “Generative adversarial networks,” *Communications of the ACM*, vol. 63, no. 11, pp. 139–144, 2020.
- [8] J. Ho, A. Jain, and P. Abbeel, “Denoising diffusion probabilistic models,” *Advances in neural information processing systems*, vol. 33, pp. 6840–6851, 2020.
- [9] T. Che, Y. Li, A. P. Jacob, Y. Bengio, and W. Li, “Mode regularized generative adversarial networks,” *arXiv preprint arXiv:1612.02136*, 2016.
- [10] R. Rombach, A. Blattmann, D. Lorenz, P. Esser, and B. Ommer, “High-resolution image synthesis with latent diffusion models,” in *Proceedings of the IEEE/CVF conference on computer vision and pattern recognition*, pp. 10684–10695, 2022.
- [11] C. Saharia, W. Chan, H. Chang, C. Lee, J. Ho, T. Salimans, D. Fleet, and M. Norouzi, “Palette: Image-to-image diffusion models,” in *ACM SIGGRAPH 2022 conference proceedings*, pp. 1–10, 2022.
- [12] J. Wang, Z. Yue, S. Zhou, K. C. Chan, and C. C. Loy, “Exploiting diffusion prior for real-world image super-resolution,” *International Journal of Computer Vision*, pp. 1–21, 2024.
- [13] P. Friedrich, J. Wolleb, F. Bieder, A. Durrer, and P. C. Cattin, “Wdm: 3d wavelet diffusion models for high-resolution medical image synthesis,” *arXiv preprint arXiv:2402.19043*, 2024.
- [14] L. Zhu, Z. Xue, Z. Jin, X. Liu, J. He, Z. Liu, and L. Yu, “Make-a-volume: Leveraging latent diffusion models for cross-modality 3d brain mri synthesis,” in *International Conference on Medical Image Computing and Computer-Assisted Intervention*, pp. 592–601, Springer, 2023.

- [15] F. Khader, G. Mueller-Franzes, S. T. Arasteh, T. Han, C. Haarbuerger, M. Schulze-Hagen, P. Schad, S. Engelhardt, B. Baessler, S. Foersch, *et al.*, "Medical diffusion: denoising diffusion probabilistic models for 3d medical image generation," *arXiv preprint arXiv:2211.03364*, 2022.
- [16] O. Ronneberger, P. Fischer, and T. Brox, "U-net: Convolutional networks for biomedical image segmentation," in *Medical image computing and computer-assisted intervention—MICCAI 2015: 18th international conference, Munich, Germany, October 5-9, 2015, proceedings, part III 18*, pp. 234–241, Springer, 2015.
- [17] W. Jin, M. Fatehi, K. Abhishek, M. Mallya, B. Toyota, and G. Hamarneh, "Applying artificial intelligence to glioma imaging: Advances and challenges," *arXiv preprint arXiv:1911.12886*, pp. 1–31, 2019.
- [18] M. D. Cirillo, D. Abramian, and A. Eklund, "Vox2vox: 3d-gan for brain tumour segmentation," in *Brainlesion: Glioma, Multiple Sclerosis, Stroke and Traumatic Brain Injuries: 6th International Workshop, BrainLes 2020, Held in Conjunction with MICCAI 2020, Lima, Peru, October 4, 2020, Revised Selected Papers, Part I 6*, pp. 274–284, Springer, 2021.
- [19] L. Sun, J. Chen, Y. Xu, M. Gong, K. Yu, and K. Batmanghelich, "Hierarchical amortized gan for 3d high resolution medical image synthesis," *IEEE journal of biomedical and health informatics*, vol. 26, no. 8, pp. 3966–3975, 2022.
- [20] G. Müller-Franzes, J. M. Niehues, F. Khader, S. T. Arasteh, C. Haarbuerger, C. Kuhl, T. Wang, T. Han, T. Nolte, S. Nebelung, *et al.*, "A multimodal comparison of latent denoising diffusion probabilistic models and generative adversarial networks for medical image synthesis," *Scientific Reports*, vol. 13, no. 1, p. 12098, 2023.
- [21] P. A. Moghadam, S. Van Dalen, K. C. Martin, J. Lennerz, S. Yip, H. Farahani, and A. Bashashati, "A morphology focused diffusion probabilistic model for synthesis of histopathology images," in *Proceedings of the IEEE/CVF winter conference on applications of computer vision*, pp. 2000–2009, 2023.
- [22] P. Guo, C. Zhao, D. Yang, Z. Xu, V. Nath, Y. Tang, B. Simon, M. Belue, S. Harmon, B. Turkbey, *et al.*, "Maisy: Medical ai for synthetic imaging," *arXiv preprint arXiv:2409.11169*, 2024.
- [23] M. Shoeybi, M. Patwary, R. Puri, P. LeGresley, J. Casper, and B. Catanzaro, "Megatron-lm: Training multi-billion parameter language models using model parallelism," *arXiv preprint arXiv:1909.08053*, 2019.
- [24] H. Chung, S. Lee, and J. C. Ye, "Decomposed diffusion sampler for accelerating large-scale inverse problems," *arXiv preprint arXiv:2303.05754*, 2023.
- [25] J. Kim and H. Park, "Adaptive latent diffusion model for 3d medical image to image translation: Multi-modal magnetic resonance imaging study," in *Proceedings of the IEEE/CVF Winter Conference on Applications of Computer Vision*, pp. 7604–7613, 2024.
- [26] P. Esser, R. Rombach, and B. Ommer, "Taming transformers for high-resolution image synthesis," in *Proceedings of the IEEE/CVF conference on computer vision and pattern recognition*, pp. 12873–12883, 2021.
- [27] A. Van Den Oord, O. Vinyals, *et al.*, "Neural discrete representation learning," *Advances in neural information processing systems*, vol. 30, 2017.
- [28] J. Johnson, A. Alahi, and L. Fei-Fei, "Perceptual losses for real-time style transfer and super-resolution," in *Computer Vision—ECCV 2016: 14th European Conference, Amsterdam, The Netherlands, October 11-14, 2016, Proceedings, Part II 14*, pp. 694–711, Springer, 2016.
- [29] A. B. L. Larsen, S. K. Sønderby, H. Larochelle, and O. Winther, "Autoencoding beyond pixels using a learned similarity metric," in *International conference on machine learning*, pp. 1558–1566, PMLR, 2016.
- [30] A. Lamb, V. Dumoulin, and A. Courville, "Discriminative regularization for generative models," *arXiv preprint arXiv:1602.03220*, 2016.
- [31] K. Simonyan, "Very deep convolutional networks for large-scale image recognition," *arXiv preprint arXiv:1409.1556*, 2014.
- [32] J. Deng, W. Dong, R. Socher, L.-J. Li, K. Li, and L. Fei-Fei, "Imagenet: A large-scale hierarchical image database," in *2009 IEEE conference on computer vision and pattern recognition*, pp. 248–255, Ieee, 2009.
- [33] W. Peebles and S. Xie, "Scalable diffusion models with transformers," in *Proceedings of the IEEE/CVF International Conference on Computer Vision*, pp. 4195–4205, 2023.
- [34] L. Zhang, A. Rao, and M. Agrawala, "Adding conditional control to text-to-image diffusion models," in *Proceedings of the IEEE/CVF International Conference on Computer Vision*, pp. 3836–3847, 2023.
- [35] S. Chilamkurthy, R. Ghosh, S. Tanamala, M. Biviji, N. G. Campeau, V. K. Venugopal, V. Mahajan, P. Rao, and P. Warier, "Development and validation of deep learning algorithms for detection of critical findings in head ct scans," *arXiv preprint arXiv:1803.05854*, 2018.
- [36] L. Wang, Q. Dou, P. T. Fletcher, S. Speidel, and S. Li, "Medical image computing and computer assisted intervention—miccai 2022," in *Proceedings of the 24th International Conference, Strasbourg, France*, vol. 12901, pp. 109–119, 2021.
- [37] H. Zheng, Y. Qin, Y. Gu, F. Xie, J. Yang, J. Sun, and G.-Z. Yang, "Alleviating class-wise gradient imbalance for pulmonary airway segmentation," *IEEE transactions on medical imaging*, vol. 40, no. 9, pp. 2452–2462, 2021.
- [38] W. Yu, H. Zheng, M. Zhang, H. Zhang, J. Sun, and J. Yang, "Break: Bronchi reconstruction by geodesic transformation and skeleton embedding," in *2022 IEEE 19th International Symposium on Biomedical Imaging (ISBI)*, pp. 1–5, IEEE, 2022.
- [39] Y. Qin, M. Chen, H. Zheng, Y. Gu, M. Shen, J. Yang, X. Huang, Y.-M. Zhu, and G.-Z. Yang, "Airwaynet: a voxel-connectivity aware approach for accurate airway segmentation using convolutional neural networks," in *International conference on medical image computing and computer-assisted intervention*, pp. 212–220, Springer, 2019.
- [40] S. G. Armato III, G. McLennan, L. Bidaut, M. F. McNitt-Gray, C. R. Meyer, A. P. Reeves, B. Zhao, D. R. Aberle, C. I. Henschke, E. A. Hoffman, *et al.*, "The lung image database consortium (lidc) and image database resource initiative (idri): a completed reference database of lung nodules on ct scans," *Medical physics*, vol. 38, no. 2, pp. 915–931, 2011.
- [41] Y. Deng, C. Wang, Y. Hui, Q. Li, J. Li, S. Luo, M. Sun, Q. Quan, S. Yang, Y. Hao, *et al.*, "Ctspine1k: a large-scale dataset for spinal vertebrae segmentation in computed tomography," *arXiv preprint arXiv:2105.14711*, 2021.
- [42] J. Ma, Y. Zhang, S. Gu, C. Zhu, C. Ge, Y. Zhang, X. An, C. Wang, Q. Wang, X. Liu, *et al.*, "Abdomenct-1k: Is abdominal organ segmentation a solved problem?," *IEEE Transactions on Pattern Analysis and Machine Intelligence*, vol. 44, no. 10, pp. 6695–6714, 2021.
- [43] C. Sudlow, J. Gallacher, N. Allen, V. Beral, P. Burton, J. Danesh, P. Downey, P. Elliott, J. Green, M. Landray, *et al.*, "Uk biobank: an open access resource for identifying the causes of a wide range of complex diseases of middle and old age," *PLoS medicine*, vol. 12, no. 3, p. e1001779, 2015.
- [44] J. Zbontar, F. Knoll, A. Sriram, T. Murrell, Z. Huang, M. J. Muckley, A. Defazio, R. Stern, P. Johnson, M. Bruno, *et al.*, "fastmri: An open dataset and benchmarks for accelerated mri," *arXiv preprint arXiv:1811.08839*, 2018.
- [45] A. Q. Nichol and P. Dhariwal, "Improved denoising diffusion probabilistic models," in *International conference on machine learning*, pp. 8162–8171, PMLR, 2021.
- [46] M. Heusel, H. Ramsauer, T. Unterthiner, B. Nessler, and S. Hochreiter, "Gans trained by a two time-scale update rule converge to a local nash equilibrium," *Advances in neural information processing systems*, vol. 30, 2017.
- [47] A. Gretton, K. M. Borgwardt, M. J. Rasch, B. Schölkopf, and A. Smola, "A kernel two-sample test," *The Journal of Machine Learning Research*, vol. 13, no. 1, pp. 723–773, 2012.
- [48] S. Chen, K. Ma, and Y. Zheng, "Med3d: Transfer learning for 3d medical image analysis," *arXiv preprint arXiv:1904.00625*, 2019.
- [49] L. Van der Maaten and G. Hinton, "Visualizing data using t-sne," *Journal of machine learning research*, vol. 9, no. 11, 2008.
- [50] Z. Wang, A. C. Bovik, H. R. Sheikh, and E. P. Simoncelli, "Image quality assessment: from error visibility to structural similarity," *IEEE transactions on image processing*, vol. 13, no. 4, pp. 600–612, 2004.
- [51] N. Heller, N. Sathianathen, A. Kalapara, E. Walczak, K. Moore, H. Kaluzniak, J. Rosenberg, P. Blake, Z. Rengel, M. Oestreich, *et al.*, "The kits19 challenge data: 300 kidney tumor cases with clinical context, ct semantic segmentations, and surgical outcomes," *arXiv preprint arXiv:1904.00445*, 2019.
- [52] W. Van Aarle, W. J. Palenstijn, J. Cant, E. Janssens, F. Bleichrodt, A. Dabrovolski, J. De Beenhouwer, K. J. Batenburg, and J. Sijbers, "Fast and flexible x-ray tomography using the astra toolbox," *Optics express*, vol. 24, no. 22, pp. 25129–25147, 2016.
- [53] A. C. Kak and M. Slaney, *Principles of computerized tomographic imaging*. SIAM, 2001.
- [54] K. H. Jin, M. T. McCann, E. Froustey, and M. Unser, "Deep convolutional neural network for inverse problems in imaging," *IEEE transactions on image processing*, vol. 26, no. 9, pp. 4509–4522, 2017.
- [55] F. Isensee, J. Petersen, A. Klein, D. Zimmerer, P. F. Jaeger, S. Kohl, J. Wasserthal, G. Koehler, T. Norajitra, S. Wirkert, *et al.*, "nnu-net: Self-adapting framework for u-net-based medical image segmentation," *arXiv preprint arXiv:1809.10486*, 2018.
- [56] J. Kim and T.-K. Kim, "Arbitrary-scale image generation and upsampling using latent diffusion model and implicit neural decoder," in *Proceedings of the IEEE/CVF Conference on Computer Vision and Pattern Recognition*, pp. 9202–9211, 2024.